Electrically Tunable Polymer Stabilized Chiral Ferroelectric Nematic Liquid Crystal Microlenses

Kelum Perera[1,2], Nilanthi Haputhantrige[1,2], Md Sakhawat Hossain[2,3], Md Mostafa[2,3], Alex Adaka[2,3], Elizabeth Mann[1,3], Oleg D. Lavrentovich[1,2,3] and Antal Jákli[1,2,3]

[1]Department of Physics, Kent State University, Kent OH, 44242, USA
[2]Advanced Materials and Liquid Crystal Institute, Kent State University, Kent OH, 44242, USA
[3]Materials Science Graduate Program, Kent State University, Kent OH, 44242, USA

Abstract

Tunable optical lenses are in great demand in modern technologies ranging from augmented and virtual reality to sensing and detection. In this work, we describe electrically tunable microlenses based on polymer stabilized chiral ferroelectric nematic liquid crystal. The power of the lens can be quickly (within 5 ms) varied by about 500 diopters by ramping an in-plane electric field from 0 to 2.5V/μm. Importantly, within this relatively low-amplitude field range, the lens is optically isotropic; thus, its focal length is independent of the polarization of incoming light. This remarkable performance combines the advantages of electrically tuned isotropic lenses and the field-controlled shape of the lens, which are unique properties of chiral ferroelectric nematic liquid crystals and have no counterpart in other liquid crystals. The achieved lens performance represents a significant step forward as compared to liquid lenses controlled by electrowetting and opens new possibilities in various applications such as biomimetic optics, security printing, and solar energy concentration.

I. Introduction

Nature developed tunable optical lenses over 500 million years ago to provide living creatures with eyes to see the environment, find mates, avoid predators, and capture prey.[1] Man-made tunable lenses using liquid crystals (LCs) have been developed starting in 1979.[2–8] A dozen years later, in 1993, electrowetting was first used to change the focal length of liquid lenses.[7,9,10]

The main reason that tunability was realized earlier for anisotropic LC lenses than for the simpler isotropic liquid lenses lies in the birefringence of the LCs. By applying an electric field

that realigns the director of molecular orientation, the effective refractive index n of a LC can be easily varied between two limiting values, $n_{\perp}$, when the director is perpendicular to the polarization of light and $n_{\parallel}$, when the director is parallel to the light polarization. This realignment changes the optical path $\xi = n \cdot d$ by a maximum of $\Delta\xi = \Delta n \cdot d$, where $\Delta n = n_{\parallel} - n_{\perp}$ is the birefringence, and d is the thickness of the LC. Switching the LC director by AC electric fields is the basis of the multibillion-dollar flat panel displays industry, and also offers an approach to planar optics lenses in which the gradients of the director and thus of n mimic the thickness variations of a conventional isotropic lens. LC lenses offer light weight, correction of astigmatisms and aberrations [4,7,11–15]. In GRIN (Gradient Index) LC lenses, a polarization-dependent spatial profile of the refractive index is created by employing a precise electrode design to apply a non-uniform electric field. Their reaction time varies with temperature and rises with the thickness of the LC layer, typically reaching a range of 10–100 milliseconds.

Tunable LC lenses can also be prepared with a fixed curved shape [2, 13-21]. In these lenses, the electric field causes director realignment and an associated change in the effective refractive index but does not change the curved shape, as first demonstrated by Sato. [2] The drawbacks of these lenses include the relatively slow response and recovery times due to the thickness of the liquid crystal layer, the sensitivity to light polarization posing challenges in certain real-world applications[16]. Different types of LC lenses of a fixed curved topography have been described in the literature: they may be tuned thermally[17,18] or electrically by imprinting the LC on curved substrates [19–22], or they may be formed by filling surface relief [23], in stacked LC layers [24] or in arrays of curved surfaces [25]. On the other hand, electric tuning of the lens shape is the defining feature of the isotropic liquid lenses controlled by the phenomenon of electrowetting [9,26,27]. Depending on the density, viscosity and surface tension of the liquids, the response time of lenses based on electro-wetting is in the order of 10–100 ms. Due to the fluidic nature of electrowetting lenses, they may be also sensitive to mechanical shocks or vibrations[16].

In this work, we show the first example of a polymer stabilized chiral ferroelectric nematic LC (FNLC) lens, providing the first LC lens with an electrically tunable shape. As compared to the electrowetting lenses, the FNLC lens can be tuned much faster and by lower voltages than of electrowetting lenses. The advantage over the conventional LC lenses is that the polymer stabilized chiral ferroelectric nematic LC lens is optically isotropic, and its performance does not depend on

the light polarization. As we will discuss, the presented unique electric tunability requires chiral and ferroelectric nematic materials and has no counterpart in conventional liquid crystals.

This work is motivated by several recent observations in chiral nematic (N^*) LCs. The first one was the observation that the N^* suspended in submillimeter size hexagonal grids and submerged in water, spontaneously forms a biconvex lens with radial variation of the optical axis.[28,29] It was found that the curvature radius that determines the focal length is proportional to the square of the helical pitch of the N^* material. It was also noted that structure of the lens array in the grid resembles compound eyes of insects; the compound eye's structure might be related to the chirality of chitin, the main component of the insects' eyes. It was also observed that a paraboloid shape plano-concave lenses can be formed in air using polymer stabilized N^* materials.[30] Even in these concave lenses the curvature radius increased within increasing N^* helical pitch.

Another important observation came after the discovery of ferroelectric nematic (N_F) LCs in 2017[31,32] using materials containing rod-shaped molecules with large dipole moments of $\sim 10\,Debye$. The N_F phase with polar order[33–35] has unique electrooptical[36–40], thermo-mechanical[41] and electro-mechanical[42] properties that may play a key role in future technological advances, such as energy storage, sensors, mechanical actuators, and displays with sub-millisecond switching. Upon doping an N_F material with chiral molecules, so that the helical pitch of the ensuing chiral ferroelectric nematic (N_F^*) is about 0.3 μm, an electrically tunable selective reflection was observed first by Feng et al[43] and later by Etxebarria et al[44]. This tuning is caused by the change of the helical pitch by an unprecedently low in-plane electric field.

The observations that the focal distance of a chiral nematic lens depends on the helical pitch, and that the pitch of a chiral ferroelectric nematic can be tuned by a small in-plane field, inspired the reported development of an LC lens based on chiral ferroelectric nematic with an in-plane electric field induced shape and thus focal length tuning.

In this paper we describe a polymer stabilized room temperature chiral ferroelectric nematic LC composite and show that it forms plano-concave lenses with the surface curvature controlled by an electric field. The observed paraboloid shape avoids spherical aberration and achieves a $\sim 500\,D$ tunable power with $5\,ms$ switching time. These features, combined with the optical isotropy of the material, represents a significant step forward as compared to isotropic liquid lenses and conventional LC lenses.

II. Results

II.A. Polymer stabilized films with interdigitated electrodes.

Figure 1 illustrates the optical and electro-optical properties of a polymer stabilized (PS) chiral ferroelectric nematic LC films of a thickness $d \approx 10\ \mu m$.

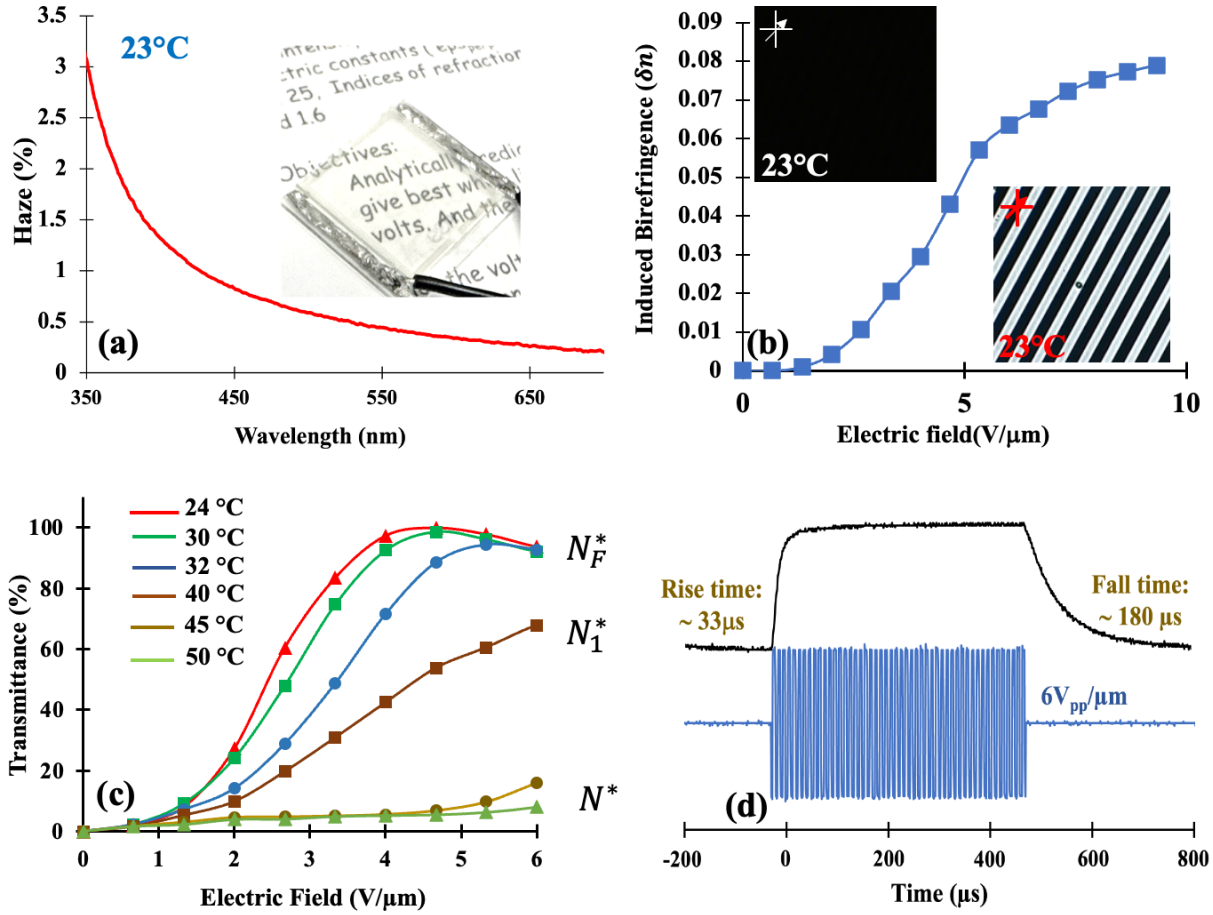

Figure 1: Optical and electro-optical properties of $\approx 10\ \mu m$ *polymer stabilized (PS) chiral ferroelectric nematic films. (a) Wavelength dependence of the haze produced by a film photopolymerized at 60°C in the isotropic phase of the* N_F^* *material; the measurements are performed at room temperature. Inset: the actual image of the cell with a text underneath to show transparency. (b) Birefringence induced by an in-plane electric field. Insets show polarized microscopy images at zero field (top-left) and at 6V/μm in-plane field applied between the interdigitated electrodes (bottom-right image). The images represent* $250\ \mu m \times 250\ \mu m$ *areas. (c) Transmittance as a function of rms electric field at different temperatures. (d) Time dependence of the optical response due to 1 kHz* $6V_{pp}/\mu m$ *rectangular field.*

As can be seen in the inset of Figure 1(a), the polymer stabilized chiral ferroelectric nematic film appears clear even at room temperature after the precursors are polymerized by UV at $60°C$ in

the isotropic phase of the N_F^* material. The haze is decreasing from 3% at 350 nm to below 1 % in the entire visible spectral range. The PS LC film is not only transparent, but also optically isotropic (dark between crossed polarizers), as seen in the top-left inset of Figure 1(b).

Upon applying an in-plane electric field **E** between interdigitated electrodes on one of the cover glasses, the texture brightens between crossed polarizers, indicating field-induced birefringence, δn. As shown in the main pane of Figure 1(b), $\delta n(E)$ increases sharply above $2.5\ V/\mu m$ and saturates above $6V/\mu m$, reaching $\delta n \approx 0.08$ at $E = 10\ V/\mu m$. This induced birefringence is more than an order of magnitude larger than that found in PS conventional nematic LCs.[45] The electric field dependence of the transmission with the electrodes at 45° with respect to the crossed polarizers at various temperatures is shown in Figure 1(c). The transmission $T = I/I_0 = sin^2[\frac{\pi \cdot \delta n \cdot d}{\lambda}]$ increases at lower temperatures and reaches the first maximum, corresponding to $\delta n \cdot d/\lambda = 1/2$, below $32°C$. In fact, the presence of this maximum gives us the opportunity to determine $\delta n(E)$ as given in Figure 1(b). Above $32°C$ the transmittance decreases considerably; we associate this with the $N_F^* - N^*$ transition, although the ferroelectric polarization could not be measured directly, since the maximum voltage we could apply did not unwind the helix with such a short (p~$0.15\ \mu m$) pitch. The switching time between the optically isotropic and birefringent states is well below a millisecond as seen in Figure 1(d). The rise time upon the application of 1 kHz$, 6\ V_{pp}/\mu m$ square wave field is $33\ \mu s$. Only ferroelectric smectic[46] and ferroelectric nematic[40] materials could show such a fast switching. Notably, the decay time back to the ground PS state is less than $200\ \mu s$. This fast relaxation is related to the small mesh size of the polymer network and to the short helical pitch.

II.B.Polymer stabilized microlens array.

The optical performance of the polymer stabilized ferroelectric nematic microlens arrays is summarized in Figure 2.

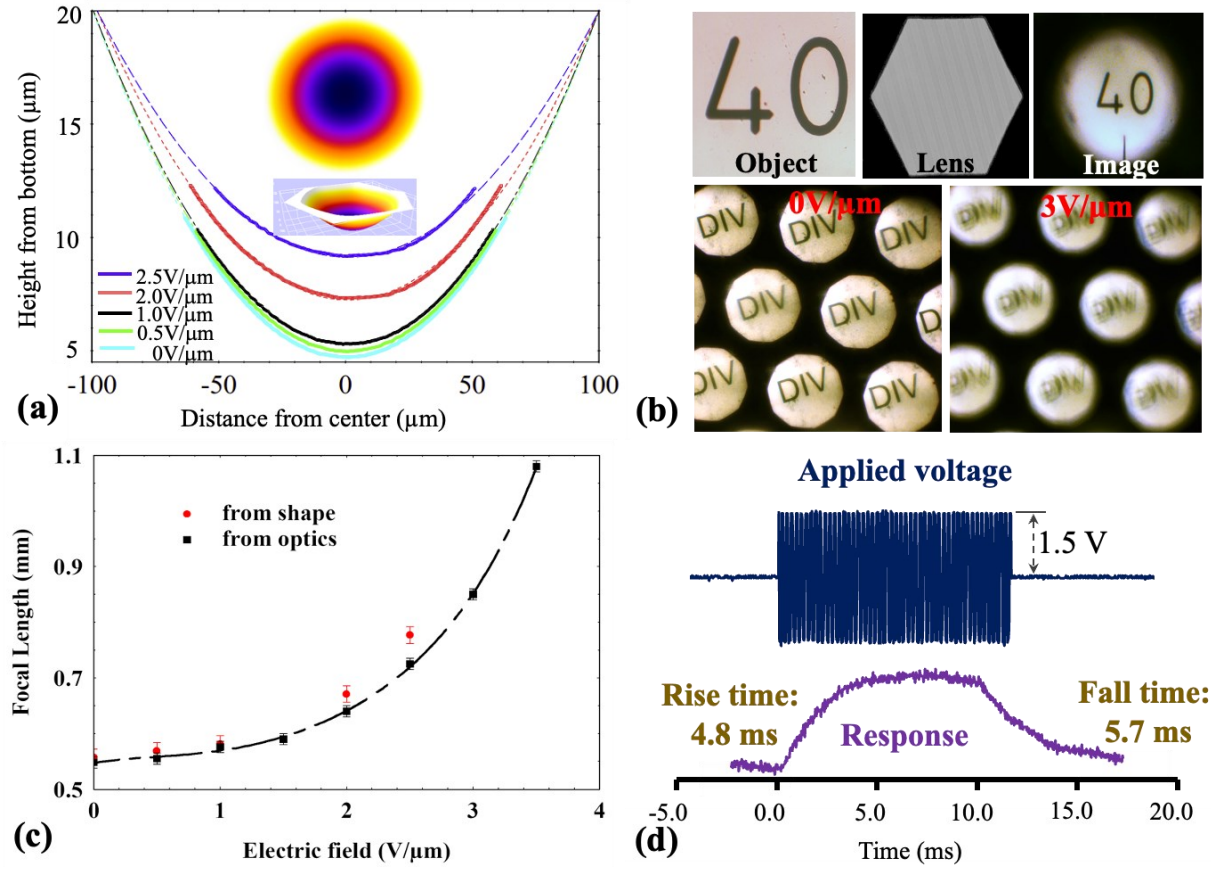

Figure 2: Optical performances of the polymer stabilized ferroelectric nematic microlens arrays at room temperature. (a) Height profile of the lens measured from the bottom as a function of the distance from the center of the hexagonal opening. The LC-air interface topography is measured by a Digital Holographic Microscope (DHM); dotted lines are the best fits using quadratic function. The lower inset shows the 3D rendering of the shape, while the upper inset with color coding shows that the lens shape remains axially symmetric when acted upon by a $2V/\mu m$ *in-plane field. (b) Optical imaging properties of the lens. Top-left image shows the object, which is a number 40; top-center image shows the hexagonal opening with interdigitated electrodes below the grid. Darker stripes correspond to the ITO electrodes and brighter stripes show non-ITO areas between the electrodes. Top-right is the reduced image of the object. Pictures in the second rows show focused and defocused images of a lens array with object "DIV" at 0and 3 V/μm 1 kHz fields. (c) Electric field dependence of the focal length. Black solid squares are the measured values deduced by the optical imaging, while solid red circles are calculated from the shape assuming effective refractive index measured in films as shown in Figure 1(b). (d) The time dependence of the defocusing and refocusing due to 1 kHz,* $6V_{pp}$ *square wave field pulse.*

Figure 2 (a) shows the height of the lens measured from the bottom as a function of the distance from the center of the hexagonal opening. The LC-air interface profile is measured by digital holographic microscope (DHM); dotted lines are the best fits using quadratic functions. One sees that the curvature is decreasing with increasing in-plane electric field in $0 - 2.5\ V/\mu m$ field range.

The lower inset shows the 3D rendering of the shape, while the upper inset with color coding shows the top view at $2V/\mu m$ in-plane field. One can see that the lens profile is axially symmetric and not biased by the electric field, i.e., the cross sections are the same when taken along different directions.

The optical imaging properties of the plano-concave lenses are illustrated in Figure 2(b). The top part shows the object (a number 40), its reduced upright image, and the picture of the hexagonal grid with interdigitated electrodes behind. Pictures in the second and third rows show defocused and refocused images of number "60", respectively at 1, 2 and 3 V/μm 1 kHz fields with the corresponding image distances using constant $\mathrm{d_o} = 3.4$ mm object distance. Figure 2(c) shows the electric field dependence of the focal length determined from the lens equation $f = \frac{d_o \cdot d_i}{d_i - d_o}$, where d_o and d_i are object and virtual image distances. The measured focal lengths have been fitted by a fifth order polynomial function. Red dots show the focal lengths calculated from the equation $f(E) \approx \frac{a^2}{2(n(E)-1)\cdot(h_c(E)-h_b(E))}$. [8] In this equation $h_b(E)$ and $h_c(E)$ are the field dependent thickness at the grid boundary (aperture) and at the center, respectively. The field-dependent refractive index $n(E)$ can be written as $n(E) = n_i + \delta n(E)$, where $n_i = \frac{n_\parallel + 2n_\perp}{3}$ is the refractive index in the optically isotropic state at zero field applied; $n_\parallel$ and $n_\perp$ are the refractive indices of the liquid crystal along and perpendicular to the director. Taking $n_\perp \approx 1.53$ and $n_\parallel = 1.75$ for FNLC 919 [47], we get $n_i \approx 1.60$. We calculated the focal length values using the shape parameters and $\delta n \approx 0$ for $E < 1.0\, V/\mu m$, δn =0.001 for $E = 2.0 \frac{V}{\mu m}$ *and* δn =0.004 for $E = 2.5 \frac{V}{\mu m}$ (see Figure 1(b)). The focal lengths calculated from the shape match those measured using the rules of geometric optics at low fields, $E < 2.5\, V/\mu m$; at higher fields, the discrepancy is about 8%, Figure 2c. This difference is likely due to the slight defocusing caused by the radial decrease of the refractive index because of the suppression of director rotation at the grid boundaries. It is important to note that, within the measurement error, the field dependence of the focal length was found to be independent of the polarization direction of the light. This is due to the optically isotropic structure at zero field and because the field-induced birefringence remains small at fields less than about $2.5V/\mu m$, Figure 1(b).

Finally, Figure 2(d) shows the time dependence of the defocusing and refocusing due to 1 kHz, $6V_{pp}$ square wave field pulse. As can be seen, both the defocusing and refocusing by about

500 $diopters$ related to the shape change of the lens take about 5 ms. These response times are much higher than the time needed for director realignment (see Figure 1(d)), but still much faster than the time $\sim 0.25\ s$ needed by a human eye to refocus just by 0.28 diopter. [48] Running a durability test for 8 million cycles did not reveal any hysteresis or change of performance.

III. Discussion

We have shown that the focal lengths of chiral ferroelectric nematic liquid crystal microlenses suspended in hexagonal grids and stabilized by polymer network in the isotropic phase, can be tuned by relatively low electric fields. The plano-concave lens is optically isotropic at zero electric field due to the random distribution of the direction of the helical axis (see Figure 3(a)). Under in-plane fields, the helix axis aligns perpendicularly to the field and its pitch increases as sketched in Figure 3(b).

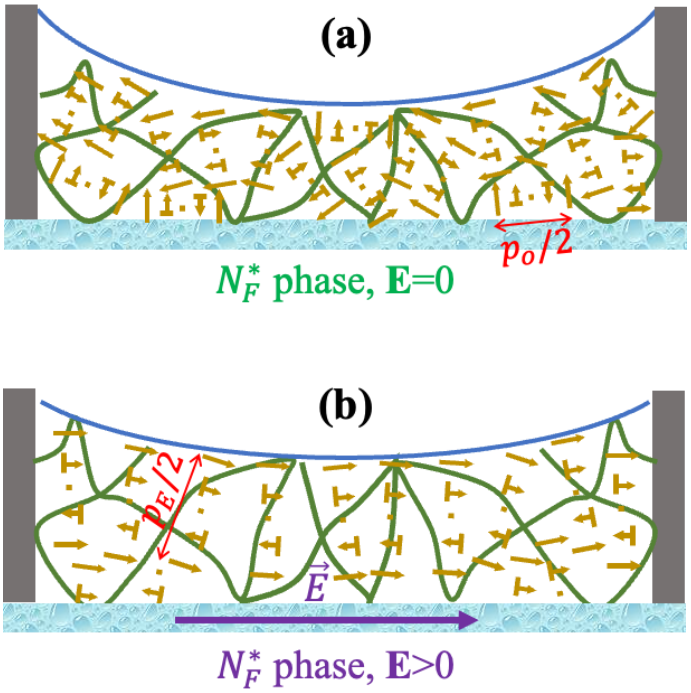

Figure 3: Sketch of the proposed nanostructure of a chiral ferroelectric nematic liquid crystal lens polymer stabilized in the isotropic phase. The polymer network is illustrated by green lines and the liquid crystal molecules are shown by ocher yellow rods. Arrows show the direction of the polarization. The head of the nail illustrates a director tilted toward the observer; p_o *and* p_E *are the helical pitch at zero field and at field E. (a) Nanostructure and shape of the lens at zero electric field; (b) Nanostructure and shape of the lens under in-plane electric field.*

The very short submicron pitch makes the field-induced birefringence practically negligible up to the field amplitude 2.5 V/μm, Figure 1(b). Because of this optical quasi-isotropy, the focal length tuned by the field in the range from 0 to $2.5\ V/\mu m$ is independent of the polarization of the incoming light. Even in such a small field range, the lens chape adjustment is so considerable that the optical power varies from $\frac{1000}{0.55} = 1818$ to $\frac{1000}{0.8} = 1250$, which is a change of over 500 diopters. In the described polymer-stabilized lens, the electrically tunable focal length is determined by the shape adjustments alone. This operational mode is different from the polarization-dependent performance of a paraboloid chiral nematic liquid crystal lens[30] that is polymer stabilized in the nematic phase with a planar alignment at the plane surface. In those paraboloid N^* lenses, the focal length depends not only by the shape geometry, but also on a Panchanaratnam-Berry – type phase.[30]

Although the in-plane field is not uniform but varies with $30\ \mu m$ periodicity of the 15 μm thick electrode and 15 μm gap, the shape does not show any periodic variation as seen in Figure 2(a). This is probably related to surface tension, which suppresses the modulation that would lead to an increase of the surface area and thus the surface energy.

Based on the observations that the focal distance of chiral nematic liquid crystal lens is determined by the helical pitch p[28,30], and the helical pitch of chiral ferroelectric nematic liquid crystals can be tuned by small in-plane fields[43], we hypothesize that the tuning we observed is related the field-induced realignment of the helical axis and the simultaneous tuning of the helical pitch of chiral ferroelectric nematic liquid crystal material.

The pseudo layering due to the helical pitch of a chiral nematic material leads to an elastic modulus $B = K_{22}\left(\frac{2\pi}{p}\right)^2$, where K_{22} is the twist elastic constant of the nematic liquid crystal. A small increase of the pitch $\delta p \ll p$ leads to a stress $\sigma_{\delta p}$

$$\sigma_{\delta p} = 4\pi^2 K_{22}\left(\frac{1}{(p+\delta p)^2} - \frac{1}{p^2}\right) \approx -8\pi^2 K_{22}\frac{\delta p}{p^3}. \quad (1)$$

The negative sign means the force is acting to decrease the curvature of the lens and it will be balanced by the stress $\sigma_{net} = Y \cdot \varepsilon$ coming from the strain ε of the polymer network with Young's modulus Y. The increase of the pitch by δp is caused by the ferroelectric stress $\mathbf{P} \cdot \mathbf{E}$, where $\mathbf{P}$ is the ferroelectric polarization and $\mathbf{E}$ is the electric field and can be expressed as

$$\delta p = \frac{P \cdot E p^3}{8\pi^2 K_{22}}. \quad (2)$$

Substituting Eq. (2) into Eq. (1), from $\sigma_{\delta p} = \sigma_{net} = Y \cdot \varepsilon$ we arrive at

$$Y \cdot \varepsilon \approx P \cdot E \tag{3}$$

The strain can be approximated by the change of the height of the lens at the center $\delta h_b = h_b(E) - h_b(0)$ divided by $\Delta h = h_c - h_b$, i.e., $\varepsilon = \frac{\delta h_b}{\Delta h} \ll 1$. From this we can estimate the electric field needed for the shape deformation as

$$E \approx \frac{Y \cdot \delta h_b}{P \cdot \Delta h} \tag{4}$$

Approximating the Young's modulus of the network as $Y \sim 1\ MPa$ and using $P \sim 6 \cdot 10^{-2} C/m^2$ at room temperature, we get $E \sim 3 \cdot 10^6 \frac{V}{m} = 3\ V/\mu m$ when $\varepsilon = 0.1$. This is indeed comparable to our results shown in Figure 2(a).

IV. Summary

In this paper we have demonstrated an array of electrically tunable polymer stabilized chiral ferroelectric nematic liquid crystal microlenses. Each lens is optically isotropic; thus, its focal length is independent of the polarization of the incoming light. The power of the lens can be switched by about 500 diopters with a few $V/\mu m$ in-plane electric fields within about 5 ms. This remarkable performance was achieved by the field-induced shape variation of the lens, which is a result of the electric field induced stresses in the polymer-stabilized chiral ferroelectric nematic. We emphasize that the role of the ferroelectric nematics is not only to reduce the operation voltages and to improve the response time. The observed tuning of the focal length via field-induced curvature variation is specific to ferroelectric nematic liquid crystals. In normal nematic liquid crystals tuning was observed only in cells with fixed shape as we discussed in the introduction. As we explained in the theoretical part of the discussion, this effect requires chiral and ferroelectric materials. The chirality leads to curved interface between the chiral nematic material and a soft (liquid or gas) surface that provides degenerate planar anchoring. The curvature radius is defined by the helical pitch; therefore, the variation of the pitch leads to shape changes. Only chiral ferroelectric nematic liquid crystals can change the pitch in the presence of very low field, and they align parallel to air. Therefore, the electric field tunable focal length is only possible by using a highly polar material in its chiral ferroelectric nematic phase. Additionally, our microlens have a parabolic cross-section profile which minimizes the spherical aberration. Finally, concave lenses are used in AR/VR devices to control the field of view, reduce aberration, and

correct near-sightedness by diverging incoming light rays, allowing the wearer to see distant virtual objects more clearly without the need for additional eyeglasses. These features make the presented observations unique and represent a significant leap compared to the electrowetting-induced tuning of liquid lenses and open new realms in various applications such as biomimetic optics, security printing, solar concentration, and AR/VR devices.

V. Materials and Methods

The explored composition represents a mixture of the 75wt% ferroelectric nematic abbreviated FNLC 919 and synthesized by Merck, with the components that form the polymeric network; the chemical structure of these components is presented in Fig.4. The preparation of the polymer stabilized lens is shown in Figure 4. FNLC 919 has two nematic phases N and N_1 above the N_F phase. The phase sequence in cooling is $I\ 80°C\ N_1\ 44°C\ N\ 32°C\ N_F\ 8°C\ Cr$. FNLC 919 was studied by Yu et al[47], who reported that at room temperature it has a birefringence $\Delta n \sim 0.22\ at\ 550\ nm$ and showed polarization peak without giving its value. Máthé et al found that the ferroelectric polarization of the pure FNLC 919 is $0.03\frac{C}{m^2}$ at room temperature[49] , which is typical for ferroelectric nematic materials. The remaining $25\ wt\%$ of the precursors contains $6\ wt\%$ chiral dopant R5011 from Daken Chemicals, Inc (helical twisting power (HTP)$\sim 112\ \mu m^{-1}$); $18\ wt\%$ photocurable monomers ($8wt\%$ TMPTA, $6wt\%$ RM 257 and $4wt\%$ EHA) and $1\ wt\%$ photoinitiator, Irgacure 651. Increasing trifunctional TMPTA will result in a stiffer network, which requires a higher voltage for a significant electric field response. Monofunctional EHA alone cannot create a stiff enough network to eliminate the residual birefringence after applying voltage. The delicate balance of polymer ratios required to optimize the performance was determined experimentally.

To fabricate the lens, we spin-coated $10\ nm$ thick polyimide PI-2555 (HD MicroSystems) layer on top of IPS10/10 substrates. Nickel Ted Pella TEM grids were cleaned in methanol with an ultrasonic cleaner (Branson B200) before use. Each cell in the double mesh is $20\ \mu m$ thick and has a side length of $a = 100\ \mu m$. The grid arrays were glued to PI 2555 coated glass substrates by applying a thin layer of "Norland 68" adhesive on the bottom of the grid cell walls and placing the grid carefully on top of the glass, avoiding any spreading of the glue on the glass and glue was cured using $365\ nm$ UV light (Black-Ray, Model B-100AP/R) for 10 minutes to permanently settle the grids on top of the PI 2555 coated glass. About $1\ \mu L$ of LC mixture was put on top of the

grid using a micropipette and compressed air with a pressure of 2 kPa was applied to the grid for $2s$ at ~45° to push a fraction of the LC out from the cells to make an underfilled state to form the Plano-concave microlenses. Then the sample was partially photopolymerized at $60°C$ in open air for 5 min using a 365 nm wavelength UV of $5mW/cm^2$ intensity. Higher intensity UV curing or expose to UV for long periods results in an increased driving voltage. The top protective cover glass was assembled with ~20 μm spacers to protect the lens array from dust.

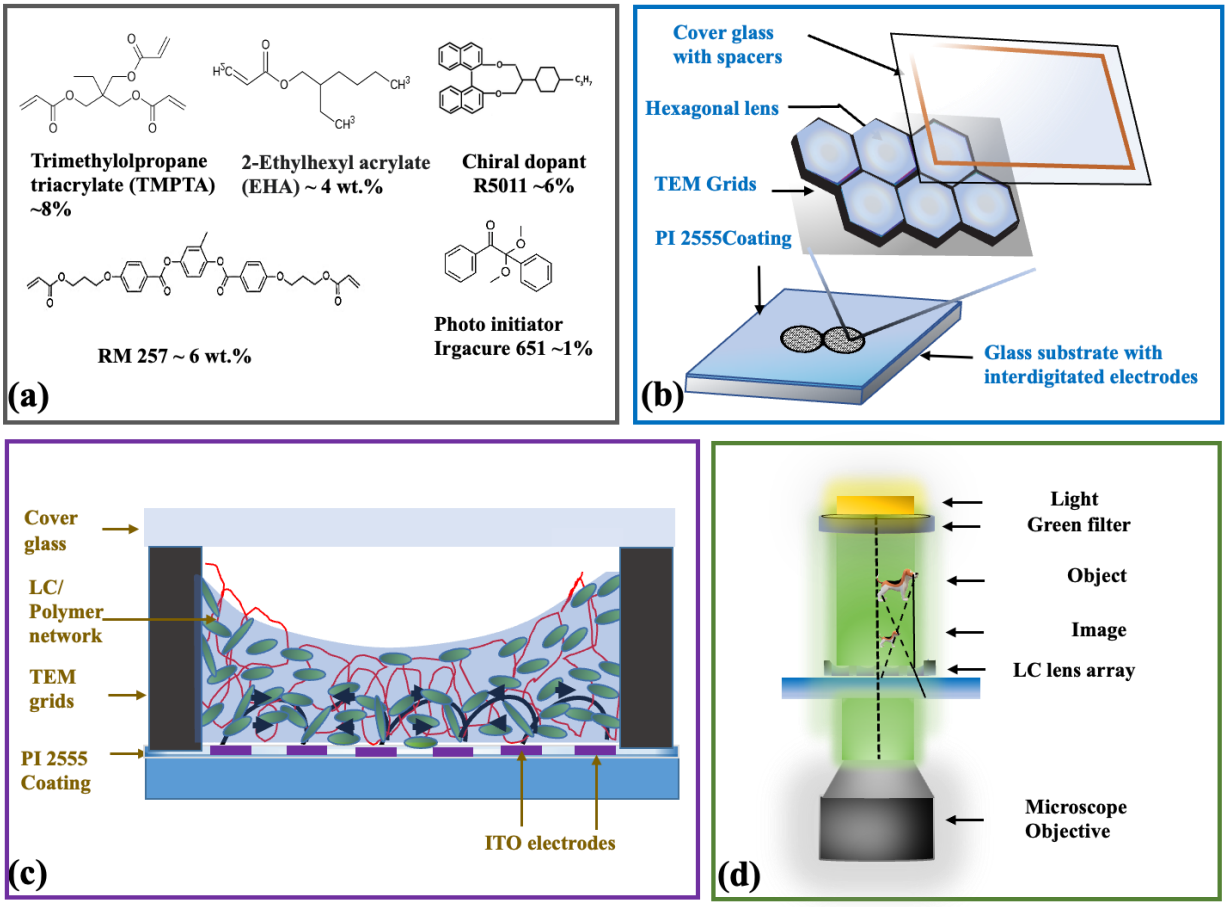

Figure 4: (a) Chemical structure of the materials used to polymer stabilize and twist the ferroelectric nematic FNLC 919 Merck ferroelectric nematic mixture and the sketch of the preparation of the microlens arrays. (b) 3D rendering of the glass substrate, TEM double mesh grids and a cover glass; (c) Sketch of the side-view of a single grid with interdigitated electrodes and the Plano-concave lens of the polymer stabilized liquid crystal covered with a glass slide. (d) Optical setup to visualize the object, image, and the lens array to measure the focal length.

To test the physical properties, the precursor was heated to $90°C$ stirred using a magnetic stirrer and then filled into an in-plane switching (IPS) cell. The 9.8 µm thick IPS cell consisted of interdigitated electrodes on the bottom substrate (IPS 15/15- electrode width $w = 15\mu m$, spacing

between electrode $l = 15\mu m$). The cell was photopolymerized for 30 min in the isotropic phase at $60°C$ using UV light (Black-Ray, Model B-100AP/R intensity $\sim 75\, mW/cm^2$) to achieve an optically isotropic polymer stabilized material.

The haze of the films was measured using an integrated sphere of a UV-3600 Plus Shimadzu UV-Vis-NIR Spectrophotometer. The haze value is calculated by the ratio of total transmittance and diffuse reflectance. First, the instrument was calibrated using a white standard plate. Then, the total light transmittance (T_t) of a sample was determined with respect to the white standard. It is followed by the measurement of the sample diffusion (T_s), while keeping only the sample inside the integrating sphere. Finally, and empty instrument diffusion (T_i) was determined. The diffuse transmittance (T_d) can be determined as $T_d = T_s - T_i\left(\frac{T_t}{100}\right)$ and the haze in percentage as $H(\%) = \frac{T_d}{T_t} \cdot 100$.

The voltage dependence of the in-plane field induced birefringence $\delta n(V)$ was measured by a home-made photodiode while the sample was placed between crossed polarizers with the IPS electrodes being 45° with respect to the polarizers. The time dependence of the variation of the intensity $I = I_0 sin^2[\frac{\pi \cdot \delta n \cdot d}{\lambda}]$ of the transmitted monochromatic light with wavelength λ provided the rise (decay) time defined as the time taken for switching between 10% and 90% (90% and 10%) of the maximum transmittance. Then the transmitted signal was detected using a photodiode connected to a Keysight InfiniiVision MSO-X-3024A digital oscilloscope.

The shape of the free surface of the polymer stabilized liquid crystal lenses has been studied by Reflection Digital Holographic Microscope (Lyncée Tec). Digital holograms of the surfaces were created using 666 nm monochromatic reference beam, which interfered with the object beam received from reflecting from the lenses. The phase images are used to get the quantitative data of 3D surface profiles with $\approx 0.3\, nm$ vertical resolution.

VI. Acknowledgement

This work was supported by NSF grants DMR-2210083 (AJ) and ECCS-2122399 (ODL). This work was completed while EKM served at the National Science Foundation. The material FNLC 919 was provided by Merck Electronics KGsA, Darmstadt, Germany. K.P. acknowledges useful discussions with Chien Tusung at National Sun Yat-sen University, Taiwan.

VII. References

[1] M. F. Land, *Current Biology* **2005**, *15*, DOI 10.1016/j.cub.2005.04.041.

[2] S. Sato, *Jpn J Appl Phys* **1979**, *18*, 1679.

[3] S. U. Kim, J. H. Na, C. Kim, S. D. Lee, *Liq Cryst* **2017**, *44*, 2121.

[4] L. Li, D. Bryant, P. J. Bos, *Liq Cryst Rev* **2014**, *2*, 130.

[5] H. C. Lin, M. S. Chen, Y. H. Lin, *Transactions on Electrical and Electronic Materials* **2011**, *12*, 234.

[6] S. Sato, *Applications of Liquid Crystals to Variable-Focusing Lenses*, **1999**.

[7] H. Ren, S. Wu, *Introduction to Adaptive Lenses*, Wiley, New York, **2012**.

[8] Y. H. Lin, Y. J. Wang, V. Reshetnyak, *Liq Cryst Rev* **2017**, *5*, 111.

[9] B. Berge, J. Peseux, *European Physical Journal E* **2000**, *3*, 159.

[10] N. T. Nguyen, *Biomicrofluidics* **2010**, *4*, DOI 10.1063/1.3460392.

[11] O. Pishnyak, S. Sato, O. D. Lavrentovich, *Appl Opt* **2006**, *45*, 4576.

[12] H. Ren, S.-T. Wu, *Opt Express* **2006**, *14*, 11292.

[13] C. T. Xu, D. W. Zhang, R. Yuan, Q. M. Chen, X. Liang, W. Hu, *Laser Photon Rev* **2023**, DOI 10.1002/lpor.202201013.

[14] C. T. Xu, P. Chen, Y. H. Zhang, X. Y. Fan, Y. Q. Lu, W. Hu, *Appl Phys Lett* **2021**, *118*, DOI 10.1063/5.0041117.

[15] J. B. Wu, S. B. Wu, H. M. Cao, Q. M. Chen, Y. Q. Lu, W. Hu, *Adv Opt Mater* **2022**, *10*, DOI 10.1002/adom.202201015.

[16] L. Chen, M. Ghilardi, J. J. C. Busfield, F. Carpi, *Front Robot AI* **2021**, *8*, DOI 10.3389/frobt.2021.678046.

[17] J. H. Kim, Y. H. Kim, H. S. Jeong, M. Srinivasarao, S. D. Hudson, H. T. Jung, *RSC Adv* **2012**, *2*, 6729.

[18] K. C. Heo, S. H. Yu, J. H. Kwon, J. S. Gwag, *Appl Opt* **2013**, *52*, 8460.

[19] J. S. Patel, K. Rastani, *Opt Lett* **1991**, *16*, 532.

[20] S. Kaur, Y.-J. Kim, H. Milton, D. Mistry, I. M. Syed, J. Bailey, K. S. Novoselov, J. C. Jones, P. B. Morgan, J. Clamp, H. F. Gleeson, *Opt Express* **2016**, *24*, 8782.

[21] H. E. Milton, P. B. Morgan, J. H. Clamp, H. F. Gleeson, *Opt Express* **2014**, *22*, 8035.

[22] I. M. Syed, S. Kaur, H. E. Milton, D. Mistry, J. Bailey, P. B. Morgan, J. C. Jones, H. F. Gleeson, *Opt Express* **2015**, *23*, 9911.

[23] L. G. Commander, S. E. Day, D. R. Selviah, *Opt Commun* **2000**, *177*, 157.

[24] M. Tanaka, S. Sato, *Japanese Journal of Applied Physics, Part 1: Regular Papers and Short Notes and Review Papers* **2002**, *41*, 5332.

[25] J. Kim, J. Kim, J.-H. Na, B. Lee, S.-D. Lee, *Opt Express* **2014**, *22*, 3316.

[26] D. Graham-Rowe, *Nat Photonics* **2006**, 2.

[27] S. Wu, H. Ren, Y.-J. Lin, M. G. J. Moharam, S.-T. Wu, N. Tabiryan, *Opt Express* **2009**, *17*, 17590.

[28] P. Popov, L. W. Honaker, M. Mirheydari, E. K. Mann, A. Jákli, *Sci Rep* **2017**, *7*, 1603.

[29] K. Perera, A. Nemati, E. K. Mann, T. Hegmann, A. Jákli, *ACS Appl Mater Interfaces* **2021**, *13*, 4574.

[30] K. Perera, H. N. Padmini, E. Mann, A. Jákli, *Adv Opt Mater* **2021**, *2101510*, 1.

[31] H. Nishikawa, F. Araoka, *Advanced Materials* **2021**, *33*, 2101305.

[32] R. J. Mandle, S. J. Cowling, J. W. Goodby, *Physical Chemistry Chemical Physics* **2017**, *19*, 11429.

[33] X. Chen, E. Korblova, D. Dong, X. Wei, R. Shao, L. Radzihovsky, M. A. Glaser, J. E. MacLennan, D. Bedrov, D. M. Walba, N. A. Clark, *Proc Natl Acad Sci U S A* **2020**, *117*, 14021.

[34] N. Sebastián, M. Čopič, A. Mertelj, *Phys Rev E* **2022**, *106*, 021001.

[35] N. Sebastián, L. Cmok, R. J. Mandle, M. R. De La Fuente, I. Drevenšek Olenik, M. Čopič, A. Mertelj, *Phys Rev Lett* **2020**, *124*, 037801.

[36] X. Zhao, J. Zhou, J. Li, J. Kougo, Z. Wan, M. Huang, S. Aya, *Proc Natl Acad Sci U S A* **2021**, *118*, e2111101118.

[37] J. Li, H. Nishikawa, J. Kougo, J. Zhou, S. Dai, W. Tang, X. Zhao, Y. Hisai, M. Huang, S. Aya, *Sci Adv* **2021**, *7*, eabf5047.

[38] R. Saha, P. Nepal, C. Feng, M. S. Hossain, M. Fukuto, R. Li, J. T. Gleeson, S. Sprunt, R. J. Twieg, A. Jákli, *Liq Cryst* **2022**, *49*, 1784.

[39] E. K. P. Rudquist D.M. Walba, R. Shao, N.A. Clark and J.E. Maclennan, *Liq Cryst* **1999**, *26*, 1555.

[40] X. Chen, E. Korblova, M. A. Glaser, J. E. Maclennan, D. M. Walba, N. A. Clark, *PNAS* **2021**, *118*, e2104092118.

[41] M. T. Máthé, Á. Buka, A. Jákli, P. Salamon, *Phys Rev E* **2022**, *105*, L052701.

[42] K. Perera, R. Saha, P. Nepal, R. Dharmarathna, M. S. Hossain, M. Mostafa, A. Adaka, R. Waroquet, R. J. Twieg, A. Jákli, *Soft Matter* **2022**, *19*, 347.

[43] C. Feng, R. Saha, E. Korblova, D. Walba, S. N. Sprunt, A. Jákli, *Adv Opt Mater* **2021**, 2101230.

[44] J. Ortega, C. L. Folcia, J. Etxebarria, T. Sierra, *Liq Cryst* **2022**, *49*, 2128.

[45] H. Ren, Y. H. Fan, S. Gauza, S. T. Wu, *Opt Commun* **2004**, *230*, 267.

[46] N. A. Clark, S. T. Lagerwall, *Appl Phys Lett* **1980**, *36*, 899.

[47] J.-S. Yu, J. H. Lee, J.-Y. Lee, J.-H. Kim, *Soft Matter* **2023**, 2446.

[48] G. Walsh, W. N. Charman, *Vision Res* **1988**, *28*, 1207.

[49] M. T. Máthé, K. Perera, Á. Buka, P. Salamon, A. Jákli, *ArXiv* **2023**, 2307.16588.